Mechanism of eIF6 release from the nascent 60S ribosomal subunit

Félix Weis[1,2,3,4], Emmanuel Giudice[5], Mark Churcher[2,3,4], Li Jin[2,3,4,6], Christine Hilcenko[1,2,3,4], Chi C. Wong[7], David Traynor[6], Robert R. Kay[6], Alan J. Warren[1,2,3,4]

[1]Cambridge Institute for Medical Research, Cambridge, UK.

[2]Medical Research Council Laboratory of Molecular Biology, University of Cambridge Research Unit, Cambridge, UK

[3]The Department of Haematology, University of Cambridge, Cambridge, UK.

[4]Wellcome Trust-Medical Research Council Stem Cell Institute, University of Cambridge, Cambridge, UK.

[5]Université de Rennes 1, Centre Nationale de la Recherche Scientifique, Unité Mixte de Recherche 6290, Institut de Génétique et Développement de Rennes, Rennes, France.

[6]Medical Research Council Laboratory of Molecular Biology, Cambridge, UK.

[7]Experimental Cancer Genetics, Wellcome Trust Sanger Institute, Cambridge, UK.

Present address

[6]Medical Research Council Laboratory of Molecular Biology, Cambridge, UK (L.J.)

Corresponding author: Alan J. Warren

Email: ajw1000@cam.ac.uk

Tel: +44 (0) 1223-2748488 Fax: +44 (0) 01223 336827

Abstract

SBDS (deficient in the inherited leukemia predisposition disorder Shwachman-Diamond syndrome) and the GTPase EFL1 (an EF-G homolog) activate nascent 60S ribosomal subunits for translation by catalyzing eviction of the anti-association factor eIF6 from nascent 60S ribosomal subunits. However, the mechanism is completely unknown. Here, we present cryo-electron microscopy structures of human SBDS and SBDS-EFL1 bound to *Dictyostelium discoideum* 60S ribosomal subunits with and without endogenous eIF6. SBDS assesses the integrity of the P-site, bridging uL16 (mutated in T-cell acute lymphoblastic leukemia) with uL11 at the P-stalk base and the sarcin-ricin loop. Upon EFL1 binding, SBDS is repositioned around helix 69, promoting a conformational switch in EFL1 that displaces eIF6 by competing for an overlapping binding site on the 60S ribosomal subunit. Our data reveal the conserved mechanism of eIF6 release that is corrupted in both inherited and sporadic leukemias.

Introduction

The nascent large (60S) ribosomal subunit undergoes an ordered series of final maturation steps in the cytoplasm to become competent to enter translation[1]. In particular, the Shwachman-Bodian-Diamond syndrome protein (SBDS, Sdo1 in *Saccharomyces cerevisiae*) that is deficient in the inherited leukemia predisposition disorder Shwachman-Diamond syndrome (SDS)[2] cooperates with the GTPase elongation factor-like 1 (EFL1, also known as EFTUD1) to catalyze eviction of the ribosome anti-association factor eukaryotic initiation factor 6 (eIF6, Tif6 in *S. cerevisiae*)[3-6]. The eIF6 protein sterically blocks formation of the B6 intersubunit bridge[7,8] by binding to the sarcin-ricin loop (SRL), uL14 and eL24 (unified nomenclature for ribosomal proteins[9]) on the 60S intersubunit face and must therefore be removed to allow the assembly of actively translating 80S ribosomes[10]. Upon release, eIF6 shuttles back to the nucleus where it plays an essential role in the biogenesis and nuclear export of the 60S ribosomal subunit[11].

SDS is characterized by poor growth, exocrine pancreatic insufficiency, skeletal abnormalities and bone marrow failure, with a 30-40% risk of progression to myelodysplastic syndrome (MDS) and acute myeloid leukemia (AML)[12]. Interestingly, a subset of T-cell acute lymphoblastic leukemias (T-ALL) are associated with recurrent uL16 mutations[13] that impair the release of Tif6 (and the 60S nuclear export adaptor Nmd3) when expressed in yeast. Together, these data support the hypothesis that defective late 60S ribosomal subunit maturation may drive leukemic transformation. However, the mechanistic link between SBDS, uL16 and eIF6 remains unclear.

Like eIF6, the SBDS protein is shared by eukaryotes and archaea. X-ray crystallography and solution NMR spectroscopy have revealed the conserved tripartite architecture of the SBDS protein[5,14-16]. Human SBDS comprises domains I (FYSH domain, residues S2-S96), II (residues D97-A170) and III (residues H171-E250). EFL1 is homologous to the ribosomal translocase EF-G in prokaryotes and to elongation factor 2 (EF-2) in eukaryotes[3]. Like E-2, EFL1 has an overall five-domain architecture, including domain I that contains the G1-G5 motifs that bind and hydrolyze GTP. Intriguingly, the ferredoxin-like fold of SBDS domain III is most closely related to domain V of EF-2, that is also found in EFL1[14]. The presence of an insertion of variable length within domain II distinguishes EFL1 from other ribosomal translocases.

To elucidate the mechanism eIF6 release from nascent 60S ribosomal subunits, we have used single particle cryo-electron microscopy (cryo-EM) to determine the structures of native *Dictyostelium discoideum* pre-60S ribosomal subunits with and without endogenous eIF6 bound to human SBDS and SBDS-EFL1. We show that dynamic rotation of the SBDS protein in the ribosomal P-site is coupled to a conformational switch in EFL1 that promotes eIF6 displacement through competition for an overlapping binding site on the 60S ribosomal subunit. Together, our data reveal the mechanism underlying a key conserved quality control step in 60S subunit maturation that is corrupted in human leukemia-associated ribosomopathies.

Results

SBDS contacts uL16 in the ribosomal P-site

To determine the mechanism of eIF6 release, we capitalized on the observation that human SBDS and EFL1 can evict eIF6 from purified native *Dictyostelium* pre-60S subunits[6]. Using single particle cryo-electron microscopy (cryo-EM) and *in silico* sorting, we determined the structures of three complexes (60S-eIF6-SBDS, 60S-eIF6-SBDS-EFL1 and 60S-SBDS-EFL1) from a single heterogeneous mixture containing the non-hydrolysable GTP analogue β, γ-methyleneguanosine 5'-triphosphate (GMPPCP), human SBDS and EFL1 and native *Dictyostelium* 60S ribosomal subunits carrying endogenous eIF6. We were able to trap eIF6 on 85% of the native pre-60S subunits by using a *Dictyostelium* strain (HM2917) that overexpresses a dominant negative SBDS-GFP fusion protein[6] (**Online methods**). A low concentration of glutaraldehyde was added to reduce preferential particle orientation on the cryo-EM grid.

We generated a 3D cryo-EM map of the 60S-eIF6-SBDS complex at 3.3 Å resolution (**Fig. 1a, b and Supplementary Fig. 2a**). Although the local resolution (**Supplementary Fig. 2b**) extends to 3 Å in some areas of the 60S-eIF6-SBDS complex, allowing unambiguous visualization of RNA bases (**Supplementary Fig. 2c**) or ribosomal protein side chains (**Supplementary Fig. 2d**), the resolution decreases towards the periphery, particularly for the bound assembly factors. In the 60S-eIF6-SBDS complex, the resolution of the SBDS protein is in the range of 4-5 Å, allowing identification of α-helices and β-sheets (**Supplementary Fig. 2e**). The maps allowed us to fit and refine homology models of *Dictyostelium* eIF6, ribosomal proteins, ribosomal RNA (rRNA) fragments and the solution NMR structure of human SBDS[5] (**Supplementary Fig. 2g-i and 3a-c and Supplementary Tables 1 and 2**).

The structure of the 60S subunit reflects that of the mature ribosome[17-19]. The eIF6 binding site is conserved, involving the C-terminus of uL14 in close proximity to the sarcin-ricin loop (SRL), the loop formed by residues 58-71 of uL3 and the N-terminus of eL24[7,8,20] (**Fig. 1c**). There is no direct contact between eIF6 and SBDS. Consistent with *in vitro* binding studies[21], SBDS domain I occupies the P-site of the 60S ribosomal subunit, packing between the P-loop (helix 80), helix 69 and the conserved essential internal loop of uL16, a ribosomal protein that is targeted by recurrent mutations (R98S, R98C and Q123P) in T-ALL[13] (**Fig. 1d**). On one face of the β-hairpin at the base of uL16, residue Q123 (*Dictyostelium* M123) lies in close proximity to SBDS domain I (helix α2). Based on the yeast 80S crystal structure[17], the side-chain of the highly conserved uL16 residue R98 on the opposite face of the hairpin, likely makes an electrostatic interaction with helix 39 (nucleotides 1363-4). SBDS residues S2-V15 interact with components of the peptidyl transferase center (PTC), the six N-terminal residues extending into the ribosomal peptide exit tunnel (**Fig. 1b**). SBDS domain III contacts the SRL (helix 95) and the P-stalk base (uL11, helices 43 and 44) in a similar manner to domain V of EF-G[22] and EF-2[23] (**Fig. 1e**). Thus, SBDS shields the active sites of the 60S subunit including the P-site, PTC, the entrance to the polypeptide exit tunnel and the binding site at the P-stalk base for the translational GTPases. Furthermore, our data reveal a direct structural link on the ribosome between SBDS (mutated in the inherited leukemia predisposition disorder SDS) and uL16 (mutated in acquired pediatric T-ALL).

EFL1 and eIF6 compete for an overlapping binding site

With no direct contact between SBDS and eIF6, we hypothesized that EFL1, like its homolog EF-2, might bind in the canonical translational GTPase center, where it might potentially interact with both SBDS and eIF6. To test this hypothesis, we obtained cryo-EM maps of complexes containing 60S-eIF6-SBDS-EFL1 (**Fig. 2a**) and 60S-SBDS-EFL1 (lacking endogenous eIF6) (**Fig. 2b**) at overall resolutions of 4.1 Å and 4.2 Å respectively (**Supplementary Fig. 2a**). The local resolution for EFL1 is in the range of 8-9 Å, limiting interpretation to protein domains (**Supplementary Fig. 2b, f**). In the absence of a high-resolution EFL1 crystal structure, we built a homology model for human EFL1 (**Online Methods and Supplementary Fig. 4a-c**) and docked this together with SBDS and eIF6 unambiguously into the cryo-EM maps (**Supplementary Fig. 2h, i and 4d-g and Supplementary Tables 1 and 2**).

EFL1 adopts two distinct conformations. In the 60S-eIF6-SBDS-EFL1 complex, consistent with competitive EF-2 binding assays[24], EFL1 binds to a site on the intersubunit face of the large subunit that is common to other canonical translational GTPases[22,25,26]. However, of the total EFL1 buried surface area (4609.3 Å^2), only 13.5% contacts rRNA, the remainder binding SBDS (33%), eIF6 (40%), uL11 (12%) and uL10 (1.5%). In transition to the 60S-SBDS-EFL1 complex, EFL1 has undergone a large-scale arc-like interdomain movement with domains I-II (~20 Å) and IV (~10 Å) pivoting around the relatively fixed axis formed by domains III and V (**Fig. 2c and Supplementary Movie 1**). EFL1 undergoes an overall "accommodation" on the 60S subunit that results in more extensive interactions with the rRNA (24% of the total buried surface area of 4762.4 Å^2), ribosomal proteins (34%) and SBDS (42%). By competing with eIF6 for an overlapping binding site on the 60S ribosomal subunit, the "accommodated" EFL1 conformation is incompatible with simultaneous binding of eIF6 (**Fig. 2d**). Specifically, in the "accommodated" state, EFL1 domain I comes into close contact with the tip of the SRL and with uL14 (**Fig. 2e, f**). Although the EFL1 domain II insertion (that distinguishes EFL1 from EF-2) also contacts eIF6, genetic complementation experiments in *S. cerevisiae* revealed that it was dispensable for *EFL1* function *in vivo* (**Supplementary Fig. 5a, b**). Furthermore, in contrast with previous reports[27,28], Tif6 residues S174 and S175 (and indeed the poorly conserved C-terminal 21 amino acids) were dispensable for Tif6 recycling *in vivo* (**Supplementary Fig. 5c, d**). We conclude that in the "accommodated" conformation, EFL1 domain I has a critical role in competing with eIF6 for the overlapping binding site on the SRL.

Dynamic rotation of SBDS

Consistent with the global domain motions observed by solution NMR spectroscopic analysis[5], SBDS domain II undergoes a 60° rotation on EFL1 binding, with a pivot point through the N-terminus of helix $\alpha 5$ (**Fig. 3a-d and Supplementary Movie 2**). SBDS domain III rotates 180° away from the P-stalk base ("closed" state) towards helix 69 ("open" state), while SBDS domain I remains anchored in the P-site. Displacement of SBDS domain III from its binding site at the P-stalk base by EFL1 domain V explains the intriguing structural homology between these two protein domains of diverse amino acid sequence[14]: SBDS and EFL1 both share a common binding site on the 60S subunit, but cannot bind simultaneously to the P-stalk base.

Interpreting disease-related SBDS variants

Due to the conservation of rRNA and ribosomal protein sequences between human and *Dictyostelium*, our structure allows us to interpret the consequences of SDS-associated disease mutations in a ribosomal context. We set out to functionally validate the importance of the potential contacts between SBDS and the ribosome observed in our cryo-EM structure by genetic complementation of *SDO1* deleted (*sdo1Δ*) yeast cells and by analyzing 60S subunit binding in an *sdo1Δ* suppressor strain (C375) that allows expression of Sdo1 variants as the sole source of Sdo1 (**Fig. 4a, b**). All three domains were required for Sdo1 function *in vivo*, domain I being necessary but not sufficient for 60S binding. Several disease-related alleles (*sdo1-F57L, N67E, K151N, K151E, R224E*) were defective in both the genetic complementation and binding assays. The F57L missense mutation perturbs the fold of SBDS domain I (but not II or III)[5]. The local resolution of the SBDS protein in the maps (4-5 Å) does not allow us to visualize individual amino acid side chains. Nevertheless, the structure suggests that the disease-associated residue K67 (yeast N67) in SBDS domain I potentially makes an electrostatic interaction with the P-loop (nucleotide G2956) (**Fig. 4c**). Consistent with this hypothesis, substitution of the *sdo1-N67E* allele with *N67G* or *N67K* restored both *sdo1Δ* cell growth and Sdo1 binding to the ribosome (**Fig. 4a, b**). Thus, a specific interaction between Sdo1 domain I and the 60S subunit is required for yeast cell fitness. Upon EFL1 binding, the highly conserved residues K151 (N-terminus of helix $\alpha 7$) and R218 (yeast R224, helix $\alpha 9$ of SBDS domain III) potentially make electrostatic interactions with the tip of helix 69 (nucleotides 2522-3) (**Fig. 4d).** Together with the genetic and biochemical analysis (**Fig. 4a, b**), our data support a key role for K151 and R218 in stabilizing the "open" conformation of the SBDS protein. Indeed, as the density for H69 is clear in our maps (the local resolution is 4-5 Å in the 60S-eIF6-SBDS complex), it is reasonable to propose that SBDS stabilizes the conformation of H69, a structural element that is usually not well ordered in isolated 60S subunits. The 60° rotation of SBDS domain II relative to domain I (**Fig. 3d**) in the presence of EFL1 involves a flexible linker (residues K90-R100) that potentially interacts with the rRNA between helices 69 and 71 (nucleotides 2551-2) (**Fig. 4e**). The functional importance of the linker is supported by the fitness defects of disease-related alleles (*sdo1-Δ94-95* and *sdo1-D97-K98delinsEVQVS*) that alter the linker length and *sdo1-R100E* that alters the charge of a highly conserved residue at the N-terminus of helix α5 (**Fig. 4a, b**). Flexibility in this region is likely important in facilitating the rotational dynamics of SBDS on the ribosome. We conclude that disease-related SBDS variants target rRNA contacts that are critical for 60S binding and the stabilization of functionally important conformational states. These data provide important *in vivo* validation of the cryo-EM structures.

Interpreting T-ALL associated uL16 variants

Mutations in uL16 (*uL16-R98S*, *R98C* and *H123P*) are recurrently associated with T-ALL and perturb Tif6 (and Nmd3) release in yeast[13]. Residue R98 of uL16 makes an electrostatic interaction with helix 39 (nucleotides 1363-4) in the crystal structure of the yeast ribosome[17]. In view of the close interaction in our structure between uL16 and SBDS in the P-site (**Fig. 1d**), we hypothesized that like *uL16-S104D*[21,29], the T-ALL associated *uL16-R98S* allele might impair Tif6 release indirectly by destabilizing the interaction of uL16 with helix 39, thereby altering the conformation of the uL16 P-site loop and reducing Sdo1 binding *in vivo*. Supporting this hypothesis, the T-ALL alleles *uL16-R98S*, *R98C* and *H123P* all impaired yeast cell fitness and 60S binding by Sdo1 *in vivo* (**Supplementary Fig. 5e-g**). However, unlike *uL16-R98S* and *R98C*, the *uL16-H123P* allele markedly reduced uL16 protein expression, causing a severe fitness defect (**Supplemental Fig. 5e**), likely as a consequence of proline-induced unfolding of the uL16 β□□β5 hairpin. We conclude that T-ALL associated uL16 mutations indirectly impair eIF6 release by reducing SBDS recruitment to nascent 60S subunits *in vivo*.

Discussion

Mechanism of eIF6 release

Our cryo-EM, biochemical and genetic analysis allows us to propose a mechanism for eIF6 release, a key conserved step in the translational activation of ribosomes that is mediated by SBDS and the GTPase EFL1 in eukaryotes and likely EF-2 in archaea (**Fig. 5a-d and Supplementary Movie 3**). We propose a cofactor-dependent conformational switching model[30] in which EFL1 initially binds to the GTPase center, in direct contact with SBDS and eIF6, in a low affinity inactive GTP-bound state (**Fig. 5b**). Competing with SBDS for an overlapping binding site, EFL1 domain V promotes a 180° rotational displacement of SBDS domain III away from the P-stalk base ("closed" state) towards helix 69 ("open" state) to adopt a conformation that is likely stabilized by interactions between SBDS residues K151 and R218 and helix 69 (**Fig. 3a-d and 4d**). We suggest that in the "open" state, SBDS drives the equilibrium of GTP-bound EFL1 towards an active high affinity ("accommodated") SRL-bound conformation that effectively competes with eIF6 for an overlapping binding site on the SRL and promotes eIF6 displacement from the 60S subunit (**Fig. 5c**). In the final step of the catalytic cycle (**Fig. 5d**), we propose that the interaction of EFL1 with the SRL promotes GTP hydrolysis, shifting the EFL1 conformational equilibrium from a high to a low-affinity ribosome binding state and promoting dissociation of both EFL1 and SBDS from the 60S subunit. However, further work is required to determine the precise timing and role of GTP hydrolysis in the mechanism of eIF6 release. It is conceivable that glutaraldehyde may have trapped the less-populated "accommodated" EFL1 state on 60S subunits lacking eIF6 (15% of the initial purified population). Nevertheless, we propose that the SRL-bound "accommodated" EFL1 state defines a functionally relevant conformation as it clearly overlaps with the eIF6 binding site. Consistent with this hypothesis, clusters of mutations in yeast EFL1 that suppress the P-site loop mutant *uL16-S104D* map to domain interfaces that are involved in the conformational change that EF-2 and EF-G undergo during translocation[29]. We hypothesize that such mutations may drive the EFL1 conformational equilibrium towards the “accommodated” state.

SBDS has been proposed as a tRNA mimic[16] that is driven into the P-site by EFL1 in a pseudo-translocation event[21,29]. However, in the absence of EFL1, SBDS binds to the 60S subunit in an extended orientation that differs completely from any previously observed for tRNA (**Fig. 1a**). We suggest that the structural mechanism of eIF6 eviction is more reminiscent of bacterial ribosome recycling by RRF and EF-G (**Fig. 5e-h**)[31-35]. SBDS binds in the 60S subunit interface cavity in an orientation that is remarkably similar to RRF on the bacterial 50S subunit (**Fig. 5f**), while SBDS and RRF undergo similar extensive interdomain rotations on the large ribosomal subunit in the presence of their respective cooperating GTPases (**Fig. 5g, h**). SBDS is a multi-tasking protein: domain I protects and potentially proofreads the peptide exit tunnel and PTC; domain II promotes EFL1 conformational switching and together with domain I mediates 60S binding and dynamic interdomain motion; domain III first shields the translational GTPase binding site at the P-stalk base and later, in the “open” conformation, promotes EFL1 conformational switching.

Final quality control assessment of the nascent 60S subunit

As the substrate for our cryo-EM studies, we used late pre-60S particles purified from *Dictyostelium* cells overexpressing a dominant-negative SBDS mutant[6]. The structure of these pre-60S particles reflects that of a mature 60S subunit[17-19] enriched for bound eIF6 (but not Nmd3), with uL16 already integrated. Loading of uL16 is critical for Nmd3 eviction[36] and for Sdo1 binding to the 60S subunit *in vivo* (**Supplementary Fig. 5f, g**). Together, these data support the hypothesis that SBDS is recruited to an eIF6-bound pre-60S particle following uL16 loading and Nmd3 removal (**Fig. 5a**), ordering eIF6 (not Nmd3[1]) release as the final step in 60S subunit maturation.

As eIF6 sterically blocks ribosomal subunit joining[8], its eviction licenses the entry of mature 60S subunits into the actively translating pool. We propose that by “proofreading” the peptide exit tunnel, the P-site and the GTPase center, SBDS and EFL1 both have key roles in coupling eIF6 release to a final quality control assessment of the integrity of the active sites of the 60S subunit, similar to the functional checkpoints that regulate translational activation of the pre-40S subunit[37,38]. Together with the structures of 60S-eIF6[7,8,20], 60S-Nmd3[39] and 60S-Arx1[40,41] complexes, our data strengthen the hypothesis that cytoplasmic pre-60S assembly factors have critical roles in structural proofreading and preventing premature translation by masking the active sites of the ribosome. The intriguing presence of a rod-shaped density in the polypeptide tunnel exit in the 60S–Arx1–Rei1 complex suggests that the tunnel itself is subjected to proofreading[40]. The presence of six N-terminal residues of the SBDS protein in the proximal part of the polypeptide exit tunnel (**Fig. 1b, d**) reinforces this concept and raises the possibility that the entire length of the tunnel may undergo proofreading during assembly. Finally, the competition between EFL1 and eIF6 for an overlapping binding site on the SRL provides an elegant mechanism to couple a quality control assessment of the functional integrity of the SRL to the last step in the EFL1 catalytic cycle (GTP hydrolysis).

The oncogenic ribosome

Our data reveal an allosteric cascade in which large-scale dynamic movements in SBDS and EFL1 link the conserved P-site loop of uL16 with eIF6. Our study links the pathogenesis of inherited (SDS) and sporadic (T-ALL) forms of leukemia in a common pathway involved in 60S subunit maturation and the translational activation of ribosomes. Interestingly, SBDS deficiency appears to promote acquired interstitial deletions of chromosome 20, encompassing the *EIF6* gene, in SDS patient bone marrow cells[42], providing a potential mechanism to suppress the defect in ribosome biogenesis by reducing the copy number of the *EIF6* gene. However, precisely how defective late 60S ribosomal subunit maturation promotes the multistep progression to MDS and leukemia and the impact of compensatory suppressor mutations in this process remain key unanswered questions.

In conclusion, our study illustrates the power of cryo-EM and *in silico* sorting of a single heterogeneous population to illuminate the mechanism underlying a dynamic and fundamental late step in 60S ribosomal subunit maturation that is corrupted in the human ribosomopathies SDS and T-ALL.

Accession codes

The cryo-EM density maps have been deposited in the Electron Microscopy Data Bank with accession numbers EMD-3145, EMD-3146 and EMD-3147. Atomic coordinates have been deposited in the Protein Data Bank, with entry codes 5an9, 5anb and 5anc.

Acknowledgements

We thank A. Johnson (University of Texas) for yeast strains; B. Trumpower (Dartmouth medical School) for providing uL16 antiserum; S. Chen, C. Savva, S. De Carlo, S. Welsch, F. De Haas, M. Vos and K. Sader for technical support with cryo-EM, G. McMullan for help in movie data acquisition, T. Darling and J. Grimmett for help with computing, A. Brown for help with refinement and S. Scheres for discussion. Supported by a Federation of European Biochemical Societies Long term Fellowship (to FW), Specialist Programme from Bloodwise [12048] (AJW), the Medical Research Council [MC_U105161083] (AJW) and [U105115237] (RRK), Wellcome Trust strategic award to the Cambridge Institute for Medal Research [100140], Tesni Parry Trust (AJW), Ted's Gang (AJW) and the Cambridge NIHR Biomedical Research Centre.

Author Contribution

FW performed sample preparation, EM data collection and image processing and model refinement. EG performed model building and fitting, MC, LJ and AJW performed genetic and biochemical experiments, CH performed protein expression and purification, CCW generated mutant *Dictyostelium* strains with advice from DT and RRK, DT and FW cultured *Dictyostelium* cells. FW and AJW designed experiments and wrote the manuscript with input from all the authors.

References

1. Lo, K.Y. *et al*. Defining the pathway of cytoplasmic maturation of the 60S ribosomal subunit. *Mol Cell* **39**, 196-208 (2010).
2. Boocock, G.R. *et al*. Mutations in SBDS are associated with Shwachman-Diamond syndrome. *Nat Genet* **33**, 97-101 (2003).
3. Senger, B. *et al*. The nucle(ol)ar Tif6p and Efl1p are required for a late cytoplasmic step of ribosome synthesis. *Mol Cell* **8**, 1363-73 (2001).
4. Menne, T.F. *et al*. The Shwachman-Bodian-Diamond syndrome protein mediates translational activation of ribosomes in yeast. *Nat Genet* **39**, 486-95 (2007).
5. Finch, A.J. *et al*. Uncoupling of GTP hydrolysis from eIF6 release on the ribosome causes Shwachman-Diamond syndrome. *Genes Dev* **25**, 917-29 (2011).
6. Wong, C.C., Traynor, D., Basse, N., Kay, R.R. & Warren, A.J. Defective ribosome assembly in Shwachman-Diamond syndrome. *Blood* **118**, 4305-12 (2011).
7. Gartmann, M. *et al*. Mechanism of eIF6-mediated inhibition of ribosomal subunit joining. *J Biol Chem* **285**, 14848-51 (2010).
8. Klinge, S., Voigts-Hoffmann, F., Leibundgut, M., Arpagaus, S. & Ban, N. Crystal structure of the eukaryotic 60S ribosomal subunit in complex with initiation factor 6. *Science* **334**, 941-8 (2012).
9. Ban, N. *et al*. A new system for naming ribosomal proteins. *Curr Opin Struct Biol* **24**, 165-9 (2014).

10. Ceci, M. *et al*. Release of eIF6 (p27BBP) from the 60S subunit allows 80S ribosome assembly. *Nature* **426**, 579-84 (2003).

11. Basu, U., Si, K., Warner, J.R. & Maitra, U. The Saccharomyces cerevisiae TIF6 gene encoding translation initiation factor 6 is required for 60S ribosomal subunit biogenesis. *Mol Cell Biol* **21**, 1453-62 (2001).

12. Donadieu, J. *et al*. Analysis of risk factors for myelodysplasias, leukemias and death from infection among patients with congenital neutropenia. Experience of the French Severe Chronic Neutropenia Study Group. *Haematologica* **90**, 45-53 (2005).

13. De Keersmaecker, K. *et al*. Exome sequencing identifies mutation in CNOT3 and ribosomal genes RPL5 and RPL10 in T-cell acute lymphoblastic leukemia. *Nature Genetics* **45**, 186-190 (2013).

14. Shammas, C. *et al*. Structural and mutational analysis of the SBDS protein family. Insight into the leukemia-associated Shwachman-Diamond Syndrome. *J Biol Chem* **280**, 19221-9 (2005).

15. Savchenko, A. *et al*. The Shwachman-Bodian-Diamond syndrome protein family is involved in RNA metabolism. *J Biol Chem* **280**, 19213-20 (2005).

16. Ng, C.L. *et al*. Conformational flexibility and molecular interactions of an archaeal homologue of the Shwachman-Bodian-Diamond syndrome protein. *BMC Struct Biol* **9**, 32 (2009).

17. Ben-Shem, A. *et al*. The structure of the eukaryotic ribosome at 3.0 A resolution. *Science* **334**, 1524-9 (2011).

18. Voorhees, R.M., Fernandez, I.S., Scheres, S.H. & Hegde, R.S. Structure of the mammalian ribosome-Sec61 complex to 3.4 A resolution. *Cell* **157**, 1632-43 (2014).

19. Khatter, H., Myasnikov, A.G., Natchiar, S.K. & Klaholz, B.P. Structure of the human 80S ribosome. *Nature* **520**, 640-5 (2015).

20. Greber, B.J. *et al*. Cryo-EM Structure of the Archaeal 50S Ribosomal Subunit in Complex with Initiation Factor 6 and Implications for Ribosome Evolution. *J Mol Biol* **418**, 145-60 (2012).

21. Sulima, S.O. *et al*. Eukaryotic rpL10 drives ribosomal rotation. *Nucleic Acids Res* **42**, 2049-63 (2014).

22. Gao, Y.G. *et al*. The structure of the ribosome with elongation factor G trapped in the posttranslocational state. *Science* **326**, 694-9 (2009).

23. Anger, A.M. *et al*. Structures of the human and Drosophila 80S ribosome. *Nature* **497**, 80-5 (2013).

24. Graindorge, J.S. *et al*. Deletion of EFL1 results in heterogeneity of the 60 S GTPase-associated rRNA conformation. *J Mol Biol* **352**, 355-69 (2005).

25. Schmeing, T.M. *et al*. The crystal structure of the ribosome bound to EF-Tu and aminoacyl-tRNA. *Science* **326**, 688-94 (2009).

26. Becker, T. *et al*. Structure of the no-go mRNA decay complex Dom34-Hbs1 bound to a stalled 80S ribosome. *Nat Struct Mol Biol* **18**, 715-20 (2011).

27. Basu, U., Si, K., Deng, H. & Maitra, U. Phosphorylation of mammalian eukaryotic translation initiation factor 6 and its Saccharomyces cerevisiae homologue Tif6p: evidence that phosphorylation of Tif6p regulates its nucleocytoplasmic distribution and is required for yeast cell growth. *Mol Cell Biol* **23**, 6187-99 (2003).

28. Ray, P. *et al*. The Saccharomyces cerevisiae 60 S ribosome biogenesis factor Tif6p is regulated by Hrr25p-mediated phosphorylation. *J Biol Chem* **283**, 9681-91 (2008).

29. Bussiere, C., Hashem, Y., Arora, S., Frank, J. & Johnson, A.W. Integrity of the P-site is probed during maturation of the 60S ribosomal subunit. *J Cell Biol* **197**, 747-59 (2012).

30. Hauryliuk, V., Hansson, S. & Ehrenberg, M. Cofactor dependent conformational switching of GTPases. *Biophys J* **95**, 1704-15 (2008).

31. Lancaster, L., Kiel, M.C., Kaji, A. & Noller, H.F. Orientation of ribosome recycling factor in the ribosome from directed hydroxyl radical probing. *Cell* **111**, 129-40 (2002).

32. Wilson, D.N. *et al*. X-ray crystallography study on ribosome recycling: the mechanism of binding and action of RRF on the 50S ribosomal subunit. *EMBO J* **24**, 251-60 (2005).

33. Gao, N., Zavialov, A.V., Ehrenberg, M. & Frank, J. Specific interaction between EF-G and RRF and its implication for GTP-dependent ribosome splitting into subunits. *J Mol Biol* **374**, 1345-58 (2007).

34. Weixlbaumer, A. *et al*. Crystal structure of the ribosome recycling factor bound to the ribosome. *Nat Struct Mol Biol* **14**, 733-7 (2007).

35. Seshadri, A., Singh, N.S. & Varshney, U. Recycling of the posttermination complexes of Mycobacterium smegmatis and Escherichia coli ribosomes using heterologous factors. *J Mol Biol* **401**, 854-65 (2010).

36. Hedges, J., West, M. & Johnson, A.W. Release of the export adapter, Nmd3p, from the 60S ribosomal subunit requires Rpl10p and the cytoplasmic GTPase Lsg1p. *EMBO J* **24**, 567-79 (2005).

37. Strunk, B.S., Novak, M.N., Young, C.L. & Karbstein, K. A translation-like cycle is a quality control checkpoint for maturing 40S ribosome subunits. *Cell* **150**, 111-21 (2012).

38. Lebaron, S. *et al*. Proofreading of pre-40S ribosome maturation by a translation initiation factor and 60S subunits. *Nat Struct Mol Biol* **19**, 744-53 (2012).

39. Sengupta, J. *et al*. Characterization of the nuclear export adaptor protein Nmd3 in association with the 60S ribosomal subunit. *J Cell Biol* **189**, 1079-86 (2010).

40. Greber, B.J., Boehringer, D., Montellese, C. & Ban, N. Cryo-EM structures of Arx1 and maturation factors Rei1 and Jjj1 bound to the 60S ribosomal subunit. *Nat Struct Mol Biol* **19**, 1228-33 (2012).

41. Bradatsch, B. *et al*. Structure of the pre-60S ribosomal subunit with nuclear export factor Arx1 bound at the exit tunnel. *Nat Struct Mol Biol* **19**, 1234-41 (2012).

42. Valli, R. *et al*. Different loss of material in recurrent chromosome 20 interstitial deletions in Shwachman-Diamond syndrome and in myeloid neoplasms. *Mol Cytogenet* **6**, 56 (2013).

Figure legends

Figure 1: SBDS shields the active sites of the 60S subunit.

(**a, b**) Crown view (**a**) and transverse section (**b**) of the cryo-EM map of the 60S-eIF6-SBDS complex, filtered to 4 Å. 60S ribosomal subunit is shown in cyan, eIF6 in yellow and SBDS in magenta. CP: central protuberance; SB: stalk base; PTC: peptidyl transferase center; N: amino terminus.

(**c, d, e**) Atomic models of the interface between the 60S ribosomal subunit and eIF6 (**c**), SBDS domain I (**d**) and SBDS domain III (**e**). 26S rRNA is shown in blue, ribosomal proteins in beige, eIF6 in yellow and SBDS in magenta. Residues R98 and M123 (human Q123) of human uL16 that are mutated in T-ALL[13], are indicated. SRL: sarcin-ricin loop.

Figure 2: EFL1 and eIF6 compete for an overlapping binding site.

(**a, b**) Crown views of the cryo-EM maps of the 60S-eIF6-SBDS-EFL1 (**a**) and 60S-SBDS-EFL1 (**b**) complexes, filtered to 6 Å. EFL1 is in dark blue. CP: central protuberance; SB: stalk base.

(**c**) Superposition of the cryo-EM densities, filtered to 6 Å (**top**) or atomic models (**bottom**) of EFL1 in the presence (grey) or absence (dark blue) of eIF6.

(**d**) The volume previously occupied by eIF6 is highlighted in yellow mesh in the 60S-SBDS-EFL1 cryo-EM map.

(**e, f**) Atomic models of the 60S-SBDS-EFL1 complex with (**e**) or without (**f**) eIF6. 26S rRNA is in blue, ribosomal proteins in beige, SBDS in magenta, EFL1 domain I in orange, EFL1 domains II-V in dark blue and eIF6 in yellow.

Figure 3: Rotational displacement of SBDS upon EFL1 binding.

(a, b, c) Top views of 60S-eIF6-SBDS (**a**), 60S-eIF6-SBDS-EFL1 (**b**) and 60S-SBDS-EFL1 (**c**) complexes. SBDS is shown in magenta, 60S subunit in cyan, eIF6 in yellow and EFL1 in dark blue. For clarity, 60S, eIF6 and EFL1 densities are shown in transparency. The uL1 protein stalk (uL1), central protuberance (CP) and P-stalk base (SB) are indicated.

(d) Superposition of the SBDS structures from the 60S-eIF6-SBDS (purple), 60S-eIF6-SBDS-EFL1 (red) and 60S-SBDS-EFL1 (black) complexes. SBDS helix $\alpha5$ is indicated.

Figure 4: Disease-related SBDS variants disrupt critical interactions with the 60S rRNA.

(**a**) Complementation of *sdo1Δ* cells by disease-related *SDO1* variant alleles. Ten-fold serial dilutions (from left to right) of the indicated strains are shown. 5-FOA: 5-fluoroorotic acid.

(**b**) Impaired 60S subunit binding of disease-related Sdo1 variants *in vivo*. FLAG-tagged Sdo1 was visualized in the supernatant (S) and pellet (P) ad uL16 was visualized in the pellet across the indicated range of NaCl concentrations by immunoblotting.

(c, d, e) Mapping disease-related SBDS residues in the 60S-eIF6-SBDS-EFL1 atomic model including K67 (**c**), K151 and R218 (**d**) and Q94-V95, D97-K98 (**e**) are indicated.

Figure 5: Mechanism of eIF6 release by SBDS and EFL1.

(**a**) SBDS (“closed” state) is recruited to a late cytoplasmic eIF6-loaded pre-60S subunit following P-stalk base assembly and uL16 recruitment.

(**b**) EFL1-GTP (or EF-2-GTP in archaea) binds directly to SBDS and eIF6 in the GTPase center, promoting rotational displacement (180º) of SBDS domain III away from the P-stalk base towards helix 69 ("open" state), stabilized by SBDS residues K151 and R218.

(**c**) GTP-bound EFL1 in the "accommodated" state competes with eIF6 for an overlapping binding site on the 60S subunit that promotes eIF6 displacement.

(**d**) Interaction of EFL1-GTP with the SRL promotes GTP hydrolysis, triggering a conformational switch in EFL1 that promotes a low-affinity ribosome binding state. SBDS and EFL1-GDP dissociate from the 60S subunit.

(**e, f, g, h**) Eukaryotic ribosome maturation is structurally reminiscent of prokaryotic ribosome recycling. Atomic models of human SBDS (left) from the 60S-eIF6-SBDS complex, ribosome recycling factor (RRF) from *Thermus thermophilus* (right) (PDB code 3j0d)[43] (**e**) and density maps of SBDS (left) and RRF (right) bound to the large ribosomal subunit in the absence (**f**) or presence (**g, h**) of EFL1 (left) or EF-G (right). The 60S subunit (60S, left; 50S, right) is in cyan, SBDS (domains I-III) and RRF (I-II) in purple, EFL1 (I-V) and EF-G (I-V) in dark blue, eIF6 in yellow. uL1, uL1 protein stalk; CP, central protuberance; SB, P-stalk base; bL12, bL12 protein stalk. Density maps for the 50S-RRF and 50S-RRF-EFG complexes were generated from PDB code 3j0d[43] and PDB code 2rdo[33] using IMAGIC-V[44].

Online Methods

Yeast strains and plasmids

S. cerevisiae strains used in this study are listed in **Supplementary Table 3** and the plasmids and primers listed in **Supplementary Tables 4 and 5** respectively. Mutations were generated by Quick-Change site-directed mutagenesis (Stratagene). For 60S binding assays, a 3xFLAG cassette was inserted at the 3' end of the *SDO1* coding sequence (**Supplementary Table 5**).

Genetic complementation assays

For random sporulation assays, double mutant *tif6Δ::KanMX4 sdo1Δ::NatMX4* cells (strain AJW3) were transformed with empty vector (pRS316) control or plasmids expressing wild type *TIF6* or *TIF6* mutants. Similarly, double mutant *efl1Δ::KanMX4 sdo1Δ::NatMX4* cells (strain SE1) were transformed with empty vector (pRS316) or plasmid pAJW2 (expressing the *EFL1Δ420-580* mutant). Diploid cells were sporulated and cultured on solid –URA medium that selects for the germination of *MAT***a** meiotic progeny carrying the indicated plasmids and contains 200 mg/mL G418 to select for *tif6Δ::KanMX4* or *efl1Δ::KanMX4* cells. Plates were incubated for 4 d at 30 ºC. Viable single colonies were spotted in 10-fold serial dilutions onto solid –URA medium for 3 days at 30 ºC. Conditional haploid (strain H1) cells *(sdo1Δ::KanMX4/pYC2[GAL10::SDO1])* were transformed with plasmids (*CEN, LEU*) expressing wild type or variant *SDO1-3xFLAG* and plated onto solid media containing 5-fluoroorotic acid (1 mg/mL) counterselection for 3-5 days at 30 ºC. For 60S binding assays, FLAG-tagged Sdo1 variants were expressed as the sole source of Sdo1 in *sdo1Δ* cells harboring a gain-of-function *TIF6* suppressor allele (strain C375, *sdo1Δ TIF6-I58T* cells) to maintain fitness. FLAG-tagged Sdo1 variants were visualized by immunoblotting with anti-FLAG antiserum (Sigma ≠A8592).

Mutant uL16 proteins were visualized by immunoblotting of extracts from strains SP103, SP106 and SP107 (**Supplementary Table 3**) after repression of endogenous uL16 (Rpl10) by the addition of glucose for 16 hr. For 60S binding studies, cells were transformed with plasmids (*CEN, URA*) expressing wild-type *SDO1-3xFLAG*. Anti-uL14 (Rpl23) antibody was obtained from Abcam (≠112587). Anti-uL16 (Rpl10) rabbit polyclonal antiserum was a kind gift from B. Trumpower (Dartmouth Medical School).

Original images of blots used in this study can be found in **Supplementary Data Set 1**.

Preparation of yeast extracts

Log phase yeast cell pellets stored at -80 ºC were thawed slowly in 1 mL of ice-cold polysome lysis buffer (10 mM Tris-HCl pH 7.4, 50 mM NaCl, 1 mM DTT, 5 mM $MgCl_2$, 0.1 mg/mL cycloheximide) with protease inhibitors (Roche) added according to manufacturers instructions. Cells were ribolyzed (Powerlyser-24, MoBio) 3x 3500 m/s for 45 s and samples cleared twice in a chilled microfuge (Eppendorf) at 13, 000 rpm for 10 min. The clarified supernatant was aliquoted and stored at -80 ºC.

Sucrose cushions

50 µL yeast extracts (5-10 OD_{260}) were layered onto a 50 µL 1.1 M sucrose cushion (1.1 M sucrose, 50 mM Tris-HCl pH 7.4, 1 mM DTT, and a range of NaCl from 0-150 mM). Samples were centrifuged (Beckmann TLA100 rotor) at 100, 000 rpm for 90 min at 4 ºC. The supernatant (including the cushion volume) was placed in a fresh

tube and 25 μL 4x protein loading dye (4x LDS Novex/Invitrogen) added. The pellet was resuspended in 125 μL 1x loading dye. After heating for 5 min at 90 ºC, 15 μL of sample was electrophoresed in a 4-12% Novex gel in MES buffer for 50 min at 200 V and immunoblotted.

SDO1 suppressor mutations

PCR was used to amplify the coding sequence for wild type *SDO1* plus 500 bp 5' and 3' of the open reading frame from yeast genomic DNA. The PCR product was cloned into vector pRS314 (*CEN, TRP*). An identical restriction site (AatII) was introduced immediately 5' and 3' of the *SDO1* open reading frame. The *SDO1* plasmid was liberated and the plasmid religated ('acceptor' plasmid). Error prone PCR (GenemorphII, Agilent Technologies) was used to mutagenize *SDO1* using primers with 50 bp of complementary sequence 5' and 3' of the *SDO1* open reading frame. The PCR product and the linearized (with AatII) acceptor plasmid were transformed into the appropriate yeast strain and suppressors selected by plating onto selective media.

Purification of *Dictyostelium* 60S ribosomal subunits carrying eIF6

Dictyostelium cells (strain HM2917[6]) were grown axenically in HL5 medium plus glucose (Formedia) in shaking suspension at 22 °C to ~1.4 × 10^6 cells/mL and treated with cycloheximide (0.1 mg/mL) (Sigma-Aldrich) for 5 minutes before harvesting by centrifugation. Cells were washed once in KK2 buffer (16.5 mM KH_2PO_4, 3.9 mM K_2HPO_4, 2 mM $MgSO_4$ and 0.1 mM $CaCl_2$) with 0.1 mg/mL cycloheximide and cells pellets were flash-cooled in liquid nitrogen and stored at -80 °C. To maintain the native eIF6 complex, mild salt conditions (100 mM K(CH_3COO) and 10 mM Mg(CH_3COO)$_2$) were used in all the steps.

Cells were resuspended in lysis buffer (50 mM HEPES-KOH pH 7.5, 100 mM K(CH_3COO), 10 mM Mg(CH_3COO)$_2$, 6 mM β-mercaptoethanol, 10% (v/v) glycerol, EDTA-free protease inhibitors (Roche), 1 mM AEBSF (Melford laboratories Ltd) and 0.1 mg/mL cycloheximide) at ~5 × 10^8 cells/mL and lysed by passing once through a 5 μm Isopore membrane filter (Millipore). The lysate was cleared by centrifugation at 16, 100 g for 15 minutes at 4 °C and ~300 μL loaded onto a 3.75 mL 10%-50% (w/v) sucrose gradient in buffer A (50 mM HEPES-KOH pH 7.5, 100 mM K(CH_3COO), 10 mM Mg(CH_3COO)$_2$, 6 mM β-mercaptoethanol) in Polyallomer 11 × 60 mm centrifuge tubes (Beckman Coulter). After centrifugation (Beckman Coulter SW60Ti rotor) at 485, 050 g for 60 minutes at 4 °C, gradients were fractionated using a Brandel gradient fractionator with continuous UV monitoring (UV-1, Pharmacia) at A_{254nm} and 60S ribosomal subunit fractions collected. 500 μL of the 60S ribosomal subunit fraction were loaded onto a 500 μL 35% (w/v) sucrose cushion in buffer A in Thickwall Polycarbonate 11 × 34 mm tubes (Beckman Coulter) and centrifuged (Beckman Coulter TLA-120.2 rotor) at 627, 379 g for 15 minutes at 4 °C. 60S ribosomal subunit pellets were resuspended in buffer A to ~0.4 μM, stored on ice and used immediately.

Preparation of ribosomal complexes for cryo-electron microscopy analysis

Recombinant human SBDS (NP_057122) and EFL1 (NP_078856) were expressed in *E. coli* and *S. cerevisiae* (strain BCY123, provided by A. Newman) respectively and purified as described[5]. Complexes were obtained by mixing 120 nM purified *Dictyostelium* 60S ribosomal subunits (85% of which carried endogenous

Dictyostelium eIF6) with 1.2 μM human SBDS and 1.2 μM human EFL1 in the presence of 0.2 mM GMPPCP (Sigma-Aldrich) for 15 minutes at room temperature, before adding 0.5% (v/v) glutaraldehyde (Sigma-Aldrich) and incubating for 10 minutes at 4 °C. Complexes were used immediately for cryo-EM grid preparation. Preliminary cryo-EM studies performed in the absence of glutaraldehyde revealed dramatic preferential orientation of the ribosomal particles on the cryo-EM grid. The resulting 3D reconstruction was distorted and showed artefacts, preventing further interpretation.

Electron microscopy

3 μL aliquots of the complexes were applied on glow-discharged holey carbon grids (Quantifoil R2/2). Grids were blotted and flash-frozen in liquid ethane using a Vitrobot automat (FEI). Data acquisition was performed under low-dose conditions on a Titan KRIOS microscope (FEI) operated at 300 kV. The dataset was recorded on a back-thinned Falcon II detector (FEI) at a calibrated magnification of x 105, 263 (resulting in a pixel size of 1.33 Å on the object scale) with a defocus range of 2-3 μm. An in-house built system was used to intercept the videos from the detector at a speed of 16 frames for the 1s exposures[45]. Data were acquired automatically using the EPU software (FEI) over two 24 h sessions with two cryo-EM grids generated from the same preparation of ribosomal complexes.

Image processing

Electron micrographs showing signs of drift or astigmatism were discarded, resulting in a dataset of 3, 844 images. 170, 581 particles were selected semi-automatically using the e2boxer routine from EMAN2[46]. Contrast-transfer function parameters were determined using CTFFIND3[47]. All 2D and 3D classifications and refinements were performed using RELION[48,49].

Reference-free 2D classification was used to discard 80S ribosomes and defective particles, resulting a dataset of 121, 751 particles selected for further analysis (**Supplementary Fig. 1**). A first refinement procedure using a 60 Å low-pass filtered empty *Dictyostelium* 60S ribosomal subunit resulted in an initial cryo-EM reconstruction, at an overall resolution of 3.8 Å, revealing a complete 60S ribosomal subunit with additional densities on the intersubunit face, especially in the P-site and around the GTPase center.

However, the map suggested heterogeneity in the stoichiometry and/or conformation of the bound factors. As the refinement is dominated by the 60S subunit, we sorted the images into subsets by doing a succession of 3D classifications with three masks delimiting areas of interest on the ribosome[50,51]. The masks were spheres or combination of spheres with a voxel value of one inside and zero outside, and a soft drop-off of two pixels. As EFL1 is an EF-2 homolog, the initial mask was applied around the EF-2 binding site on the 60S subunit and the particles sorted into six classes (A1-6). Classes A5 and A6 (~16, 000 and ~12, 000 particles respectively) showed clear density for EFL1 in two distinct conformations and were processed separately. Following 3D refinement, class A6 contained densities corresponding to a 60S-eIF6-SBDS-EFL1 complex. As class A5 showed heterogeneity around the eIF6 binding site, a second mask was applied to the area encompassing eIF6 and part of EFL1 domain II and particles sorted into four classes (B1-4). 3D refinement of the main class (B3, ~10, 000 particles) yielded a map of the 60S-SBDS-EFL1 complex. The maps obtained from classes lacking EFL1 (A1 to A4, ~94, 000 particles) showed clear density for eIF6 and additional partial densities in the ribosomal P-site and P-stalk base. Consistent with a preliminary study in which purified recombinant SBDS protein alone was incubated with 60S ribosomal subunits, we ascribed the latter densities to SBDS. A third mask was applied in this area and particles sorted into six classes (C1-6). 3D refinement of the main class (C4, ~43, 000 particles) yielded a map of the 60S-eIF6-SBDS complex.

To further increase the resolution of the three classes, statistical movie processing was performed as described[45]. Reported overall resolutions (3.3 Å for the 60S-eIF6-SBDS complex, 4.1 Å for the 60S-eIF6-SBDS-EFL1 complex and 4.2 Å for the 60S-SBDS-EFL1 complex) were calculated using the gold-standard FSC = 0.143 criterion[52] and were corrected for the effects of a soft mask on the FSC curve using high-resolution noise substitution[53] (**Supplementary Fig. 2a**). The final density maps were corrected for the modulation transfer function of the detector and sharpened by applying a negative B factor that was estimated using automated procedures[54].

Modeling of ribosomal RNA fragments

Dictyostelium 26S rRNA (GenBank: FR733594.1) was aligned against the sequences of *Tetrahymena thermophila* (GenBank: JN547815.1) and *S. cerevisiae* (GenBank: JQ277730.1) 26S rRNAs using ClustalW2[55]. Based on the sequence alignment, we chose the crystal structure of the *T. thermophila* 60S ribosomal subunit in complex with initiation factor 6 (PDB code 4A18)[8] as a template, except the L1 stalk region (H76, H77, H78, and a portion of H76) for which the *S. cerevisiae* ribosome structure (PDB code 3U5H)[17] was used. The homology model of the rRNA fragments (A1221-A1270, C1356-C1602, A2392-U2700 and A2925-C3480, see **Supplementary Fig. 3a**) surrounding the SBDS binding site was constructed using both Assemble2[56] and Coot[57].

Protein Modeling

The human SBDS atomic coordinates where taken from PDB file 2L9N[5]. The sequence of *Dictyostelium* ribosomal proteins uL3 (L3), uL6 (L9), uL10 (P0), uL11 (L12), uL14 (L23), uL16 (L10), eL24 (L24), eL40 (L40) were retrieved from the Ribosomal Protein Gene Database [http://ribosome.med.miyazaki-u.ac.jp], *Dictyostelium* eIF6 and the human EFL1 sequences from the NCBI Protein database [www.ncbi.nlm.nih.gov/protein]. All the proteins were modeled by homology using the I-TASSER server[58,59]. In each case, the model with the best C-score was selected to build the final structure (**Supplementary Table 6**). Note that the lower score obtained for the EFL1 model can be explained by the size of the protein and the presence of both a large insertion domain (compared with EF-2 and EF-G) and numerous extra loop regions that had to be modeled *ab-initio* by the I-Tasser server.

Model building

To build the initial model of the 60S-eIF6-SBDS complex, we used UCSF Chimera[60] to rigid-body dock the *T. thermophila* 60S ribosomal subunit in complex with initiation factor 6 (PDB code 4A18)[8] into the 60S-eIF6-SBDS complex cryo-EM density map. Taking advantage of the high sequence similarity between the two organisms, we used this structure as our reference to align the *Dictyostelium* ribosomal RNA fragments and the uL3, uL6, uL10, uL11, uL14, uL16, eL24, eL40 and eIF6 proteins using Chimera's MatchMaker tool. In a final step, the human SBDS structure was rigid-body fitted into the cryo-EM density map. We used a similar approach to build the 60S-eIF6-SBDS-EFL1 model using the refined 60S-eIF6-SBDS atomic model as the starting conformation, and rigid-body fitting the human EFL1 homology model into the cryo-EM density maps. The 60S-SBDS-EFL1 was built in a same fashion, using the refined 60S-eIF6-SBDS-EFL1 atomic model (without eIF6) as the starting conformation.

Model fitting and refinement

Due to the intermediate resolution of the bound factors, we first used molecular dynamic flexible fitting (MDFF) to fit the NMR structure of human SBDS (pdb code 2L9N)[5] or homology models for EFL1, eIF6 and the ribosome. For optimal fitting of the models into the EM density map, we used REFMAC v5.8 adapted for EM refinement[61].

The initial system was prepared using VMD[62]. To preserve the secondary structure of the proteins, the ψ and φ dihedral angles of the amino-acid residues in α-helices or β-sheets were harmonically restrained using a force constant of 200 $\text{kcal.mol}^{-1}.\text{rad}^{-2}$. The hydrogen bonds involving backbone atoms from the same residues were maintained through the MDFF procedure[63]. For this, we used a force constant of 50 $\text{kcal.mol}^{-1}.\text{Å}^{-2}$ to restrain the distance between the acceptor and the hydrogen atom, and a force constant of 50 $\text{kcal.mol}^{-1}.\text{rad}^{-2}$ to maintain the angle formed by the donor, the hydrogen, and its acceptor. We also restrained the cis peptides into their current configurations with a force constant of 200 $\text{kcal.mol}^{-1}.\text{rad}^{-2}$ and the chiral centers to their current handedness with a force constant of 50 $\text{kcal.mol}^{-1}.\text{rad}^{-2}$. In the same way, the helical parts of the rRNA were preserved using two 200 $\text{kcal.mol}^{-1}.\text{Å}^{-2}$ restraints to maintain the distance between paired bases, and a set of 200 $\text{kcal.mol}^{-1}.\text{rad}^{-2}$ restraints to maintain the dihedral angles.

The model was optimized by MDFF *in vacuo* using NAMD[64], the CHARMM22 CMAP-corrected parameters[65] for the protein, the CHARMM27 parameters for the nucleic acids[66], and a 0.3 kcal/mol scaling factor to adjust the influence of the cryo-EM map on the model. A multiple time-step integration scheme was used to calculate bonded interactions every femtosecond, and non-bonded interactions every two femtoseconds. A cut-off distance of 10 Å was used for the non-bonded interactions. A dielectric constant of 80 was applied to adjust electrostatic interactions, and the temperature was maintained using a Langevin thermostat with a damping coefficient of 5 ps^{-1}.

To optimize fitting of the less well-defined elements of our model, the MDFF procedure was performed following a multi-step protocol. First, we performed 10, 000 steps of minimization followed by a slow heating to 300 K over the course of 20, 000 simulation steps, then 1 ns of molecular dynamic (MD) simulation, all while holding the ribosomal RNA fragments and proteins still. This allowed the SBDS fitting to improve while maintaining the position of the other components of our model that were already well placed in the cryo-EM density map. We repeated this procedure twice (10, 000 steps of minimization, 20, 000 steps of thermalization, and 1ns of MD), freeing first the ribosomal proteins and then the whole system. To improve the overall quality of the 60S-eIF6-SBDS atomic model, we finished by performing 1, 000 steps of minimization.

A similar protocol was used for the 60S-eIF6-SBDS-EFL1 and 60S-SBDS-EFL1 models. However, since the optimization protocol was performed in cascade (the MDFF-refined 60S-eIF6-SBDS atomic model was used as the starting conformation to build the 60S-eIF6-SBDS-EFL1 model and the resulting structure used as the starting conformation for the 60S-SBDS-EFL1 model), only three steps were necessary as the ribosomal RNA fragments and proteins were for the most part already well-fitted in the electron density map. We performed 10, 000 steps of minimization, a slow heating to 300 K over the course of 20, 000 simulation steps, and 1 ns of MD simulation to optimize the fitting of EFL1, all while holding the rest of the system fixed. We repeated this procedure, this time allowing the entire system to adjust into the cryo-EM density map. We used 1, 000 steps of minimization to improve the quality of the atomic models.

Masked areas of the cryo-EM density maps into which the models had been built were used for refinement in REFMAC v5.8[61]. $FSC_{average}$ was monitored during refinement to follow the fit to density, and the final models were validated using MolProbity (**Supplementary Table 1**)[67]. For cross-validation against over-fitting, the atoms of our final models were randomly displaced (with an RMSD of 0.5 Å) and a refinement procedure was performed against the maps that were reconstructed from only one of the two independent halves of the data used in our gold-standard FSC procedure. FSC curves were calculated between the resulting models and the half-maps against which they had been refined (FSC_{work}), as well as the FSC curve between those models and the other half-maps (FSC_{test}). The absence of overfitting of the models is demonstrated by the observation that the FSC_{work} and FSC_{test} curves nearly overlap (**Supplementary Fig. 2g-i**). Contact analysis was performed using VMD[62] and the Protein, Interfaces, Surfaces and Assemblies service at the European Bioinformatics Institute (http://www.ebi.ac.uk/pdbe/prot_int/pistart.html)[68]. UCSF Chimera was used for visual analysis and creating figures and movies[60].

Methods-only references

43. Yokoyama, T. *et al*. Structural insights into initial and intermediate steps of the ribosome-recycling process. *EMBO J* **31**, 1836-46 (2012).

44. van Heel, M., Harauz, G., Orlova, E.V., Schmidt, R. & Schatz, M. A new generation of the IMAGIC image processing system. *J Struct Biol* **116**, 17-24 (1996).

45. Bai, X.C., Fernandez, I.S., McMullan, G. & Scheres, S.H. Ribosome structures to near-atomic resolution from thirty thousand cryo-EM particles. *Elife* **2**, e00461 (2013).

46. Tang, G. *et al*. EMAN2: an extensible image processing suite for electron microscopy. *J Struct Biol* **157**, 38-46 (2007).

47. Mindell, J.A. & Grigorieff, N. Accurate determination of local defocus and specimen tilt in electron microscopy. *J Struct Biol* **142**, 334-47 (2003).

48. Scheres, S.H. A Bayesian view on cryo-EM structure determination. *J Mol Biol* **415**, 406-18 (2012).

49. Scheres, S.H. RELION: implementation of a Bayesian approach to cryo-EM structure determination. *J Struct Biol* **180**, 519-30 (2012).

50. Klaholz, B.P., Myasnikov, A.G. & Van Heel, M. Visualization of release factor 3 on the ribosome during termination of protein synthesis. *Nature* **427**, 862-5 (2004).

51. Penczek, P.A., Frank, J. & Spahn, C.M. A method of focused classification, based on the bootstrap 3D variance analysis, and its application to EF-G-dependent translocation. *J Struct Biol* **154**, 184-94 (2006).

52. Scheres, S.H. & Chen, S. Prevention of overfitting in cryo-EM structure determination. *Nat Methods* **9**, 853-4 (2012).

53. Chen, S. *et al*. High-resolution noise substitution to measure overfitting and validate resolution in 3D structure determination by single particle electron cryomicroscopy. *Ultramicroscopy* **135**, 24-35 (2013).

54. Rosenthal, P.B. & Henderson, R. Optimal determination of particle orientation, absolute hand, and contrast loss in single-particle electron cryomicroscopy. *J Mol Biol* **333**, 721-45 (2003).

55. Larkin, M.A. *et al*. Clustal W and Clustal X version 2.0. *Bioinformatics* **23**, 2947-8 (2007).

56. Jossinet, F., Ludwig, T.E. & Westhof, E. Assemble: an interactive graphical tool to analyze and build RNA architectures at the 2D and 3D levels. *Bioinformatics* **26**, 2057-9 (2010).

57. Emsley, P., Lohkamp, B., Scott, W.G. & Cowtan, K. Features and development of Coot. *Acta Crystallogr D Biol Crystallogr* **66**, 486-501 (2010).

58. Zhang, Y. I-TASSER server for protein 3D structure prediction. *BMC Bioinformatics* **9**, 40 (2008).

59. Roy, A., Kucukural, A. & Zhang, Y. I-TASSER: a unified platform for automated protein structure and function prediction. *Nat Protoc* **5**, 725-38 (2010).

60. Pettersen, E.F. *et al*. UCSF Chimera--a visualization system for exploratory research and analysis. *J Comput Chem* **25**, 1605-12 (2004).

61. Amunts, A. *et al*. Structure of the yeast mitochondrial large ribosomal subunit. *Science* **343**, 1485-9.

62. Humphrey, W., Dalke, A. & Schulten, K. VMD: visual molecular dynamics. *J Mol Graph* **14**, 33-8, 27-8 (1996).

63. Trabuco, L.G., Villa, E., Mitra, K., Frank, J. & Schulten, K. Flexible fitting of atomic structures into electron microscopy maps using molecular dynamics. *Structure* **16**, 673-83 (2008).

64. Phillips, J.C. *et al*. Scalable molecular dynamics with NAMD. *J Comput Chem* **26**, 1781-802 (2005).

65. Mackerell, A.D., Jr., Feig, M. & Brooks, C.L., 3rd. Extending the treatment of backbone energetics in protein force fields: limitations of gas-phase quantum mechanics in reproducing protein conformational distributions in molecular dynamics simulations. *J Comput Chem* **25**, 1400-15 (2004).

66. MacKerell, A.D., Jr., Banavali, N. & Foloppe, N. Development and current status of the CHARMM force field for nucleic acids. *Biopolymers* **56**, 257-65 (2001).

67. Chen, V.B. *et al*. MolProbity: all-atom structure validation for macromolecular crystallography. *Acta Crystallogr D Biol Crystallogr* **66**, 12-21 (2010).

68. Krissinel, E. & Henrick, K. Inference of macromolecular assemblies from crystalline state. *J Mol Biol* **372**, 774-97 (2007).

Figure 1

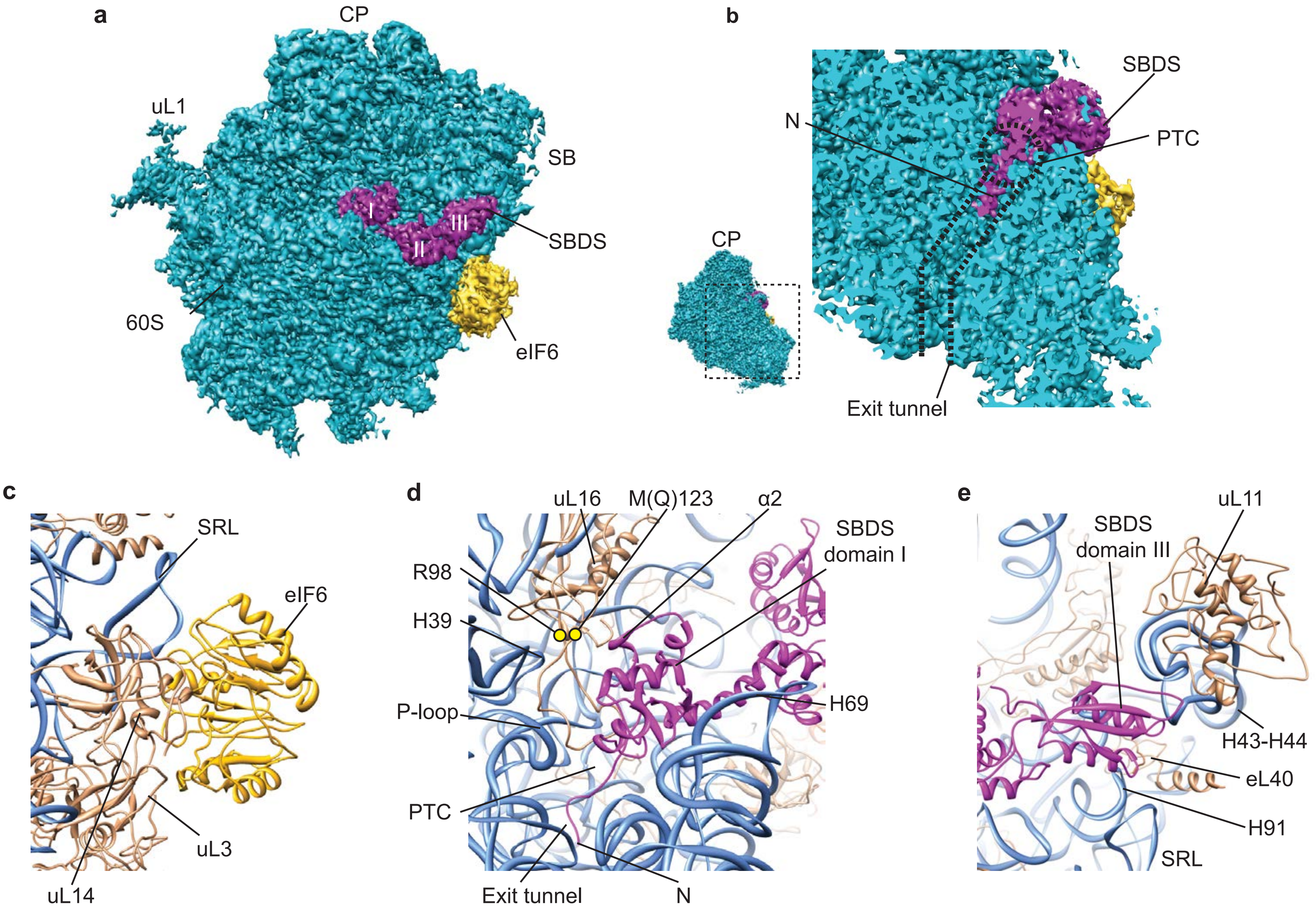
a
CP
uL1
SB
I
III
II
SBDS
60S
eIF6
b
SBDS
N
PTC
CP
Exit tunnel
c
SRL
eIF6
uL3
uL14
d
uL16
M(Q)123
α2
SBDS
domain I
R98
H39
H69
P-loop
PTC
Exit tunnel
N
e
uL11
SBDS
domain III
H43-H44
eL40
H91
SRL

Figure 2

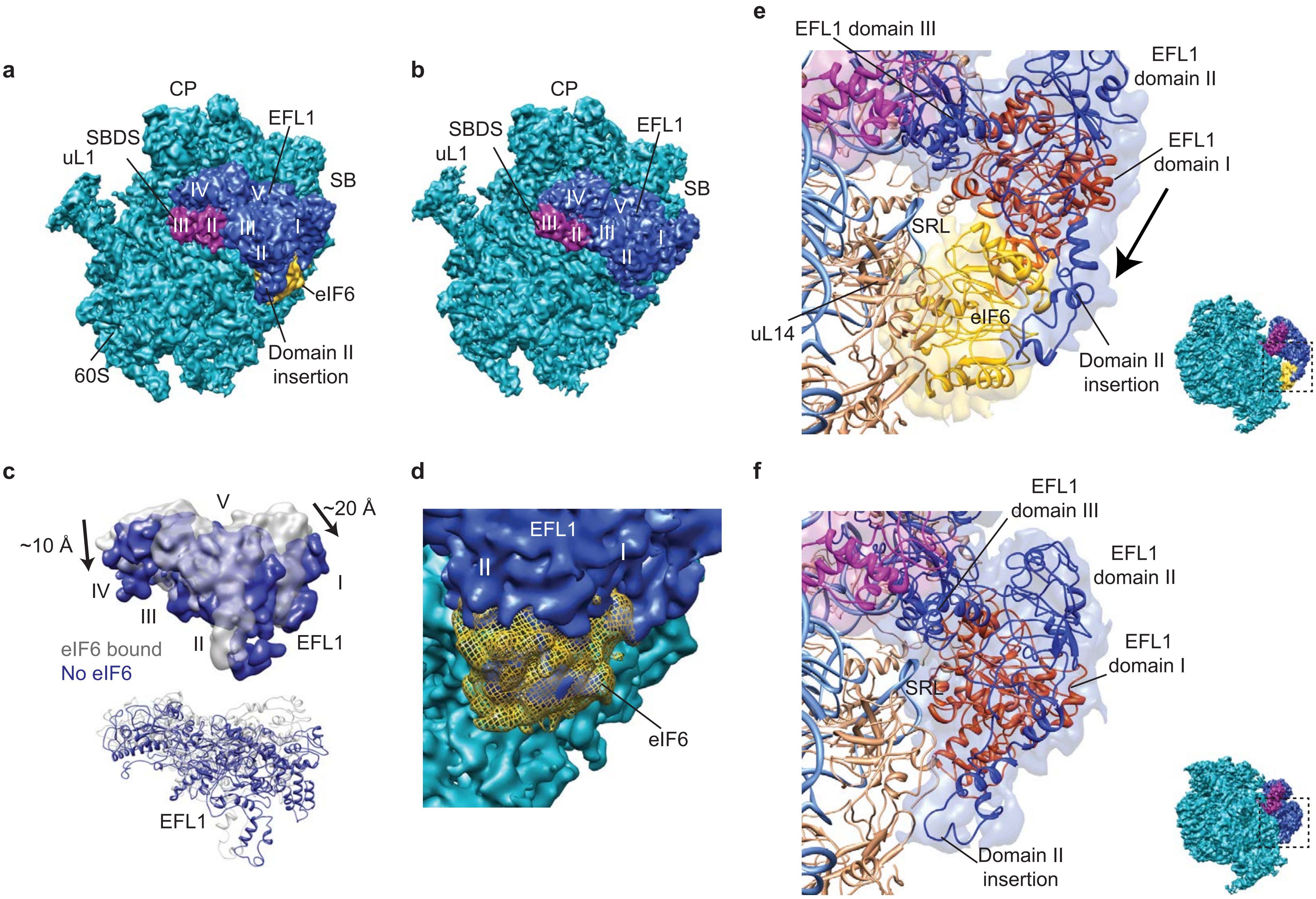
a
CP
SBDS
uL1
EFL1
SB
IV
V
III
II
III
I
II
eIF6
Domain II insertion
60S
b
CP
SBDS
uL1
EFL1
SB
IV
V
III
II
III
I
II
c
V
~20 Å
~10 Å
IV
III
II
I
EFL1
eIF6 bound
No eIF6
EFL1
d
EFL1
II
I
eIF6
e
EFL1 domain III
EFL1 domain II
EFL1 domain I
SRL
uL14
eIF6
Domain II insertion
f
EFL1 domain III
EFL1 domain II
EFL1 domain I
SRL
Domain II insertion

Figure 3

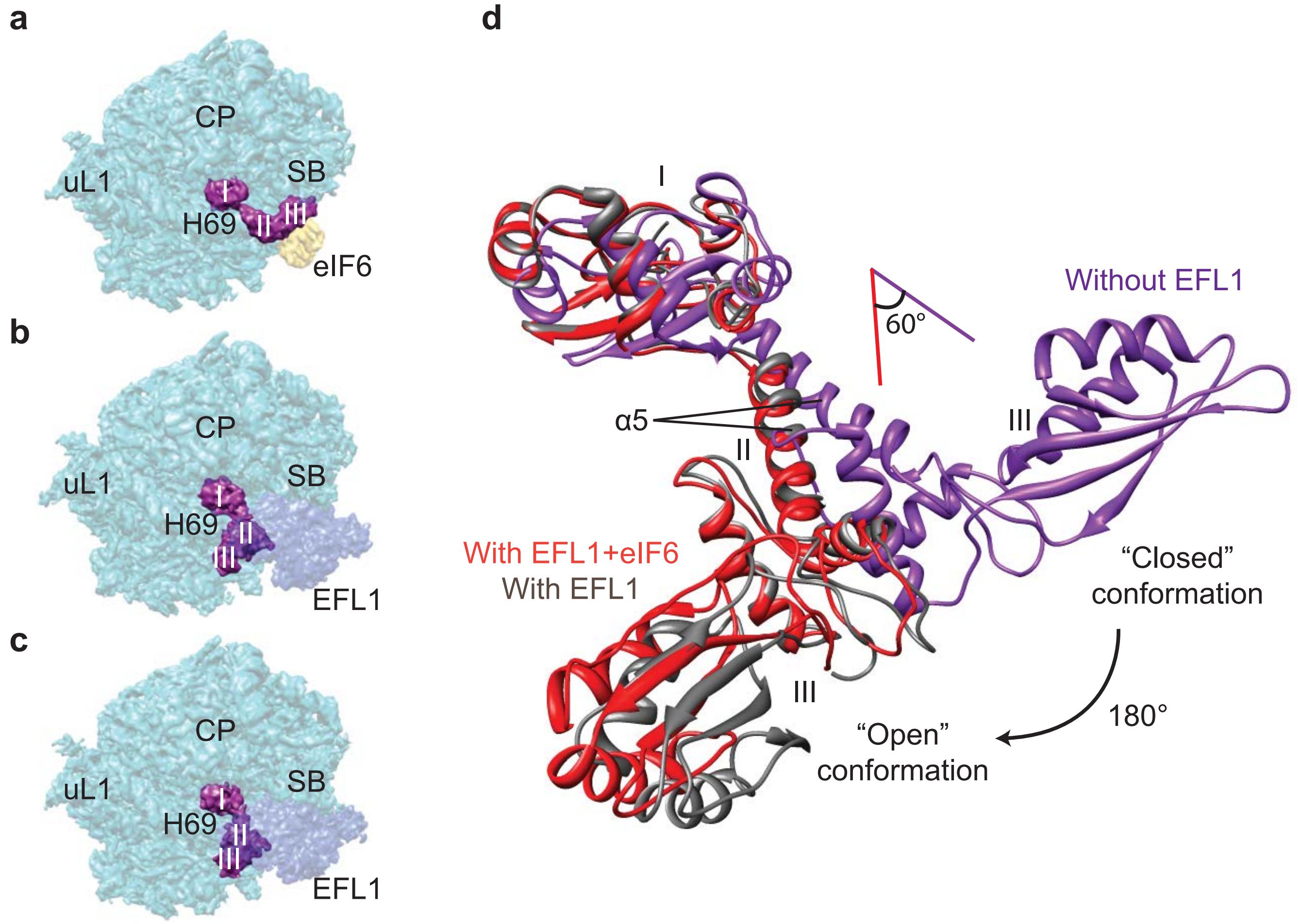
a
CP
uL1
SB
I
H69
II
III
eIF6
b
CP
uL1
SB
I
H69
II
III
EFL1
c
CP
uL1
SB
I
H69
II
III
EFL1
d
I
60°
Without EFL1
α5
II
III
With EFL1+eIF6
With EFL1
"Closed"
conformation
III
180°
"Open"
conformation

Figure 4

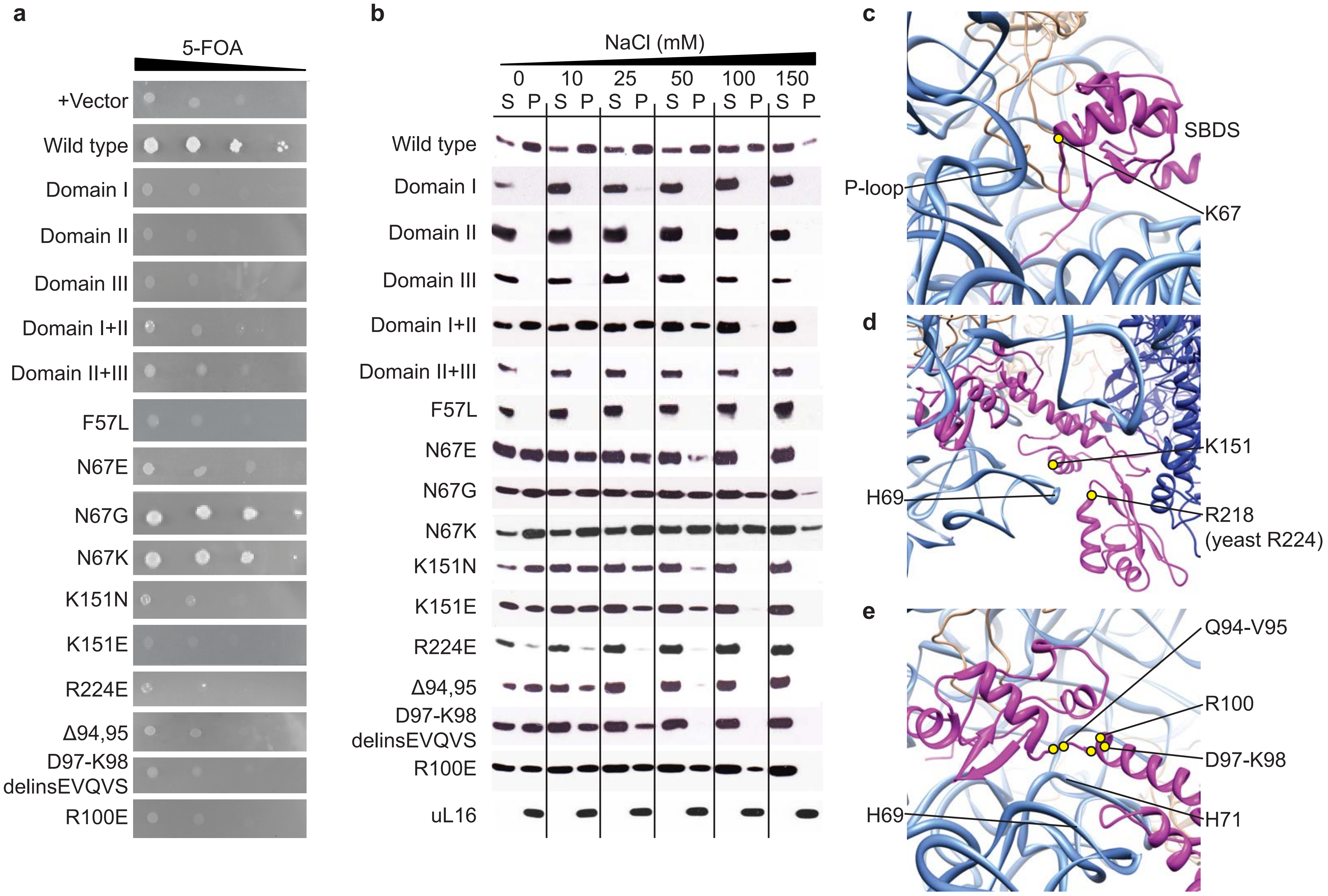
a
5-FOA
+Vector
Wild type
Domain I
Domain II
Domain III
Domain I+II
Domain II+III
F57L
N67E
N67G
N67K
K151N
K151E
R224E
Δ94,95
D97-K98
delinsEVQVS
R100E
b
NaCl (mM)
0
10
25
50
100
150
S P S P S P S P S P S P
Wild type
Domain I
Domain II
Domain III
Domain I+II
Domain II+III
F57L
N67E
N67G
N67K
K151N
K151E
R224E
Δ94,95
D97-K98
delinsEVQVS
R100E
uL16
c
SBDS
P-loop
K67
d
K151
H69
R218
(yeast R224)
e
Q94-V95
R100
D97-K98
H69
H71

Figure 5

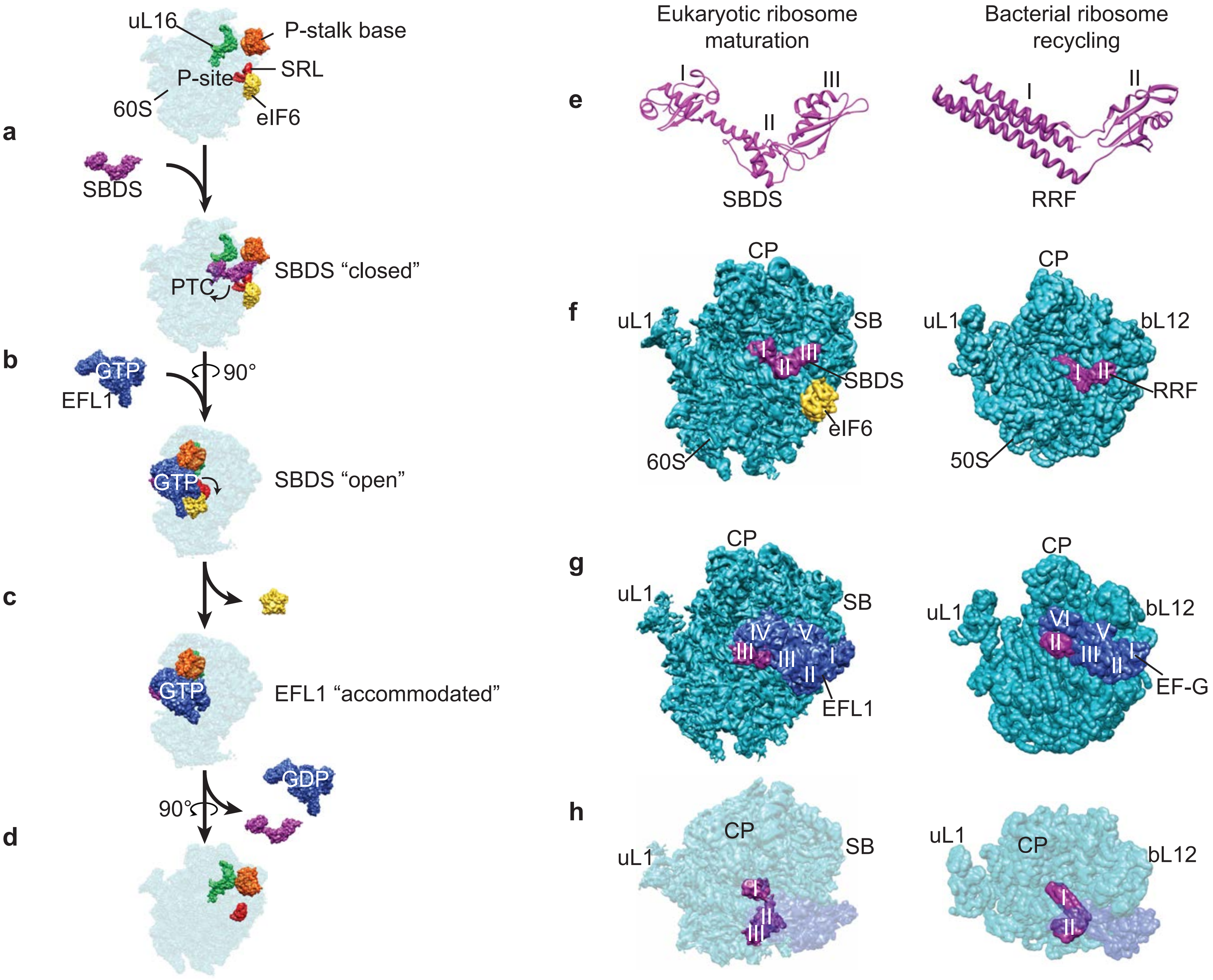
a
uL16
P-stalk base
SRL
P-site
60S
eIF6
SBDS
SBDS "closed"
PTC
b
GTP
EFL1
90°
SBDS "open"
GTP
c
EFL1 "accommodated"
GTP
GDP
90°
d
Eukaryotic ribosome maturation
Bacterial ribosome recycling
e
I
III
II
SBDS
I
II
RRF
f
CP
uL1
SB
I
III
II
SBDS
eIF6
60S
CP
uL1
bL12
I
II
RRF
50S
g
CP
uL1
SB
IV
V
III
III
I
II
EFL1
CP
uL1
bL12
VI
V
II
III
I
II
EF-G
h
CP
uL1
SB
I
II
III
uL1
CP
bL12
I
II